HHS Public Access

Author manuscript

Magn Reson Med. Author manuscript; available in PMC 2020 June 30.

Published in final edited form as:

Magn Reson Med. 2019 March ; 81(3): 1849–1862. doi:10.1002/mrm.27543.

Magnetic resonance fingerprinting with quadratic RF phase for measurement of T_2* simultaneously with δ_f, T_1, and T_2

Charlie Yi Wang[1], **Simone Coppo**[2], **Bhairav Bipin Mehta**[2], **Nicole Seiberlich**[1,2], **Xin Yu**[1,2], **Mark Alan Griswold**[1,2]

[1]Department of Biomedical Engineering, Case Western Reserve University, Cleveland, Ohio

[2]Department of Radiology, Case Western Reserve University, Cleveland, Ohio

Abstract

Purpose: This study explores the possibility of using a gradient moment balanced sequence with a quadratically varied RF excitation phase in the magnetic resonance fingerprinting (MRF) framework to quantify T_2* in addition to δ_f, T_1, and T_2 tissue properties.

Methods: The proposed quadratic RF phase-based MRF method (qRF-MRF) combined a varied RF excitation phase with the existing balanced SSFP (bSSFP)-based MRF method to generate signals that were uniquely sensitive to δ_f, T_1, T_2, as well as the distribution width of intravoxel frequency dispersion, Γ. A dictionary, generated through Bloch simulation, containing possible signal evolutions within the physiological range of δ_f, T_1, T_2, and Γ, was used to perform parameter estimation. The estimated T_2 and Γ were subsequently used to estimate T_2*. The proposed method was evaluated in phantom experiments and healthy volunteers (N = 5).

Results: The T_1 and T_2 values from the phantom by qRF-MRF demonstrated good agreement with values obtained by traditional gold standard methods (r^2 = 0.995 and 0.997, respectively; concordance correlation coefficient = 0.978 and 0.995, respectively). The T_2* values from the phantom demonstrated good agreement with values obtained through the multi-echo gradient-echo method (r^2 = 0.972, concordance correlation coefficient = 0.983). In vivo qRF-MRF-measured T_1, T_2, and T_2* values were compared with measurements by existing methods and literature values.

Conclusion: The proposed qRF-MRF method demonstrated the potential for simultaneous quantification of δ_f, T_1, T_2, and T_2* tissue properties.

Keywords

magnetic resonance fingerprinting; multiparametric mapping; quantitative MRI; T_2*

Correspondence Mark Alan Griswold, Departments of Biomedical Engineering and Radiology, Case Western Reserve University & University Hospitals of Cleveland, MRI Research – Bolwell B121, 1110 Euclid Ave., Cleveland, OH 44106. mag46@case.edu.

CONFLICT OF INTEREST

The authors receive research support from Siemens Healthineers.

1 | INTRODUCTION

Transverse relaxation time T_2* is an MR tissue property that provides insight into underlying tissue physiology and pathology. The clinical value of such insight has led to the incorporation of T_2* contrast-dependent methods such as MR-SWI and BOLD contrast-based techniques within various clinical protocols. The T_2* tissue property is affected by tissue iron concentration, making it sensitive to iron containing blood products, and has been observed to change in several disease states. Parkinson's disease is associated with increased iron in the substantia nigra, globus pallidus, and hippocampus.[1–4] Alzheimer's disease has been associated with increased iron stores in the basal ganglia, as well as hippocampal and cortical regions of the brain.[1,5,6] Huntington's disease has been associated with increased iron concentration in the globus palladus and putamen.[3] Outside of the brain, T_2*-sensitive techniques are used to monitor iron overload of the liver and heart in transfusion-dependent patients.[7,8] Iron nanoparticle-based MR contrast agents have also been engineered for versatile biological specificity that rely on MR T_2*-sensitive methods for detection.[9]

Empirically, T_2* is the exponential decay time constant of the tissue MR signal. This time constant can be decomposed into two components described by the following relationship:

$$\frac{1}{T_2^*} = \frac{1}{T_2} + \frac{1}{T'_2} \quad (1)$$

where T_2 is the time constant of non-refocusable transverse magnetization decay, and T'_2 is the time constant of refocusable transverse magnetization decay arising from intravoxel frequency dispersion. Although both T_2 and T'_2 properties are affected by tissue iron concentrations, neither property alone is specific to pathologies affecting tissue iron.[10] For example, T_2 is also affected by tissue water content, and T'_2 is also affected by macroscopic field inhomogeneities and other sources of tissue susceptibility.[8] Thus, MR methods capable of simultaneous quantification of T_2, T'_2, and T_2* properties may provide greater sensitivity and specificity to pathology. For this reason, methods such as the GESFIDE (Gradient-Echo Sampling of Free Induction Decay and Echo)[11] sequence have been developed. These methods require relatively long acquisition times because they must sample both refocused and non-refocused signal echoes, and as a result, have not yet gained widespread adoption.

Magnetic resonance fingerprinting (MRF) is a recently developed framework for the simultaneous quantification of multiple tissue properties.[12] In its initial implementation, the framework was applied to reduce quantification time for brain tissue T_1 and T_2 relaxation properties by incorporating spatial and temporal incoherence to transient signals in a balanced SSFP-based pulse sequence (bSSFP-MRF).[12] Other MRF implementations have since been developed to increase measurement robustness,[13] be applied to other organ systems,[14,15] or quantify additional tissue properties.[16,17] Application of the MRF framework to T_2* quantification may enable fast and robust quantification of T_2* along with other tissue properties within a clinical exam. However, the initially proposed bSSFP-MRF method has only slight T_2* sensitivity.[18]

This work introduces the novel quadratic RF phase-based MRF (qRF-MRF) method for the robust measurement of tissue T_2* simultaneously with tissue T_1, T_2, and off-resonance (δ_f)

properties within a single acquisition. The method was adapted from the original bSSFP-MRF method because of its sensitivity to T_1, T_2, and off-resonance (δ_f) properties.[12] The qRF-MRF T_2* sensitivity is obtained using a varied RF phase scheme that is able to generate both high signal amplitude and signal dependence to intravoxel variations in δ_f. These properties are exploited to generate unique signal evolutions with high SNR within the MRF framework for robust and rapid quantification.

2 | THEORY

Traditional bSSFP experiments have a well-characterized amplitude and phase behavior.[19,20] Typical acquisition parameters in bSSFP experiments include constant high flip angle (FA), constant short TR, constant (linear) increment in RF excitation phase (PH), and zero net gradient moment per TR. The signal observed from isochromats are highly dependent on the relative RF phase increment, defined as the difference between the PH increment and the phase accumulated over the duration of a TR due to δ_f precession.

Figure 1A shows the amplitude and phase profiles for isochromats with different relative RF phase increments. When using large flip angles, isochromats with a relative RF phase increment approximately equal to an odd multiple of π have high amplitudes and similar phase values at sampling time TE. Signals from such isochromats are coherent during bSSFP experiments, regardless of the presence or absence of δ_f variations, due to their similar phase values. Without sensitivity to δ_f variations, the generated signals by these isochromats are not sensitive to T'_2. Isochromats with relative phase increments close to an even multiple of π behave differently. Such isochromats have a steep phase profile, allowing for δ_f variation-dependent signal attenuation through phase cancelation. However, these isochromats have low signal amplitude, and signals from them cannot be reliably detected. Without signal regimes with both high amplitude and steep phase profile, the traditional bSSFP experiment is not sensitive to T'_2, and therefore is not appropriate for T_2* quantification.

Adjustments to the typical acquisition parameters during a bSSFP experiment can substantially increase T'_2 sensitivity. Figure 1B shows the amplitude and phase profiles corresponding to a bSSFP experiment with a low FA and a reduced number of preparation pulses. Here, isochromats with an even multiple of π RF phase increment maintain the steep phase profile necessary for generation of T_2*-weighted signal through intravoxel signal dephasing, but will transiently develop a large transverse amplitude before its steady state. In fact, this amplitude may surpass 50% of M_0, even greater than those encountered in traditional bSSFP experiments.

Approaches using such acquisition parameters for T_2*-weighted signal generation in bSSFP experiments have been explored previously.[21] These approaches depend on the selection of acquisition parameters such that the resulting δ_f frequencies with steep phase profile coincide with the imaging regions of interest. The δ_f frequencies associated with this band, with the potential for T_2*-weighted signal generation, is dependent on the choice of PH and TR used. Since PH and TR may be varied across imaging frames within an experiment, the frequency positions of this band, during the n_{th} frame, is approximately given by

$$\delta_{f(n)} \approx \frac{PH_{(n)} - PH_{(n-1)} - 2N\pi}{TR_{(n)} * 2\pi}, \quad (2)$$

where N is any integer. As traditional bSSFP experiments use constant PH and TR parameters, the resulting band is also constant. The T_2* sensitive regimes may be limited due to the macroscopic field inhomogeneity would the imaging FOV. By using a varied PH or TR between frames, the band can vary accordingly and allow for greater FOV coverage.

In the proposed method, a quadratic RF phase increment was selected such that PH was constantly varied. As a result, high-amplitude T_2*-weighted signal bands were swept through different δ_f values. Figure 1C shows the transient amplitude and phase profiles of an experiment with a quadratic RF phase, demonstrating preserved high amplitude and steep phase characteristics necessary for T'_2 and T_2* sensitivity. In this way, macroscopic field inhomogeneity would not limit the sensitive FOV.

3 | METHODS

3.1 | Pulse sequence design

The proposed acquisition strategy used in qRF-MRF is based on a bSSFP-type sequence with a varied FA, TR, and PH. Pulse sequence FAs, TRs, and PHs were selected to generate unique signal shapes for combinations of δ_f, T_1, T_2, and intravoxel frequency dispersion properties within clinically relevant ranges. Figure 2A–C shows the FAs, TRs, and PHs used in the proposed method. Because bSSFP-MRF already fulfills both pulse sequence design criteria for the subset of δ_f, T_1 and T_2 properties, the initial 900 time frames of the proposed qRF-MRF method were performed using the identical FA, TR, and PH scheme as the bSSFP-MRF method,[12] organized into 3 "bSSFP blocks" of 300 frames each.

For the remaining frames, a new scheme of acquisitions, using seven repeated "qRF blocks" dedicated toward intravoxel frequency dispersion sensitivity, was performed by using low FA with quadratically varied PH increment. The FA pattern (Figure 2A) of each qRF block consisted of a smoothly varied base shape that ranged from 0°–6° for odd-numbered blocks, and 0°–12° for even-numbered blocks. The qRF blocks used a constant 11.5-ms TR (Figure 2B). Within the first and second halves of each qRF block, the PH (Figure 2C) of the piecewise n_{th} frame is given by

$$PH(n) = -1.24 * n^2 + 180n \quad (3)$$

and

$$PH(n) = -1.24 * n^2 - 180n, \quad (4)$$

respectively. Each qRF block consisted of only 293 frames to reduce repetition of combinations of the sampled gradient trajectory with the FA, TR, and PH acquisition parameters used throughout the method. Finally, 49 frames, acquired with 0° FA excitation, were appended to the end of the sequence, such that a total of 3000 frames were acquired in the method, consistent with the bSSFP-MRF method.

Figure 2D shows the corresponding frequency positions of T_2*-sensitive bands during different frames of the method, as calculated by Eq. (2). These bands remain relatively stationary near ≈ ±40 Hz during the initial 900 frames, where constant alternated RF phase is used. Minor fluctuations in the position of resonance bands during these frames occurs as a result of the variations in TR. However, isochromats with δ_f values near bands during these frames develop the signal voids typically associated with bSSFP null-bands due to the relatively high FA. After the qRF blocks are initiated, the bands linearly traverse the full span of possible δ_f values. During these frames, isochromats develop transverse magnetization amplitude during particular frames, depending on δ_f value, an example of which is shown in Figure 2E. For frames in which a band traverses through a given isochromat's δ_f value, a high transverse magnetization is developed.

A variable-density spiral trajectory[22] designed with zeroth-moment and first-moment nulling was used to acquire data. The spiral trajectory required 24 and 48 interleaves to fully sample the inner and outer region of k-space, respectively. One spiral interleaf was sampled each frame, resulting in highly undersampled k-space data per frame. Previous MRF methods used a constant rotation of 7.5° of the spiral trajectory between frames to obtain spatial incoherence. In the current method, incoherence was further increased by adopting a bit-reversed ordering of sampled spiral interleafs that repeated itself every 48 frames. All acquisitions were single slice with FOV = 300 × 300 mm^2, matrix size = 256 × 256 (in-plane pixel size of 1.2 × 1.2 mm^2), and slice thickness of 5 mm. All 3000 frames for each single 2D slice were acquired in 35 seconds.

3.2 | Dictionary

A dictionary-based approach was used to perform parameter estimation for δ_f, T_1, T_2, and T_2* properties from undersampled image frame data following reconstruction. The dictionary used for parameter estimation was generated in two steps. First, a base dictionary, $S_{base}(n, \delta_f, T_1, T_2$, describing the signal at each of the 3000 frames, n, for different combinations of δ_f, T_1 and T_2 values, was simulated using the Bloch equation as described previously.[12] This base dictionary was calculated for a wide range of 421 possible δ_f values, 89 possible T_1 values, and 99 possible T_2 values. Values for δ_f ranged from ±70 Hz with 0.33-Hz step size. Values for T_1 ranged from 50 ms to 3700 ms with a variable step size, in which each value was 5% greater than the value immediately smaller than it. Values for T_2 ranged from 5 ms to 135 ms with a constant step size of 3 ms, and then 135 ms to 2000 ms with a variable step size, each with a value 5% greater than the value immediately smaller than it.

This base dictionary was then convolved by a shape function, $L(\delta_f, \Gamma)$, to generate the full dictionary, $S(n, \delta_f, T_1, T_2, \Gamma)$, such that

$$S(n, \delta_f, T_1, T_2, \Gamma) = \left(S_{base}(n, \delta_f, T_1, T_2) * L(\delta_f, \Gamma)\right)[\delta_f]. \quad (5)$$

In the current work, the shape function was limited to a Lorentzian distribution, parameterized by the Γ value that represents the FWHM of the distribution as described by

$$L(\delta_f, \Gamma) = \frac{\frac{\Gamma}{2}}{{\delta_f}^2 + \left(\frac{\Gamma}{2}\right)^2} . \quad (6)$$

Although the Lorentzian distribution may not precisely reflect the underlying distribution in vivo, this shape was chosen such that the pulse sequence simulation of a gradient-echo (GRE)-type pulse sequence would generate a monoexponentially decaying transverse signal evolution. Curve-fitting this simulated signal evolution would yield the decay time constant, T_2*, given by

$$\frac{1}{T_2^*} = \frac{1}{T_2} + \pi\,\Gamma . \quad (7)$$

Shapes, given by $L(\delta_f, \Gamma)$, were generated for 52 different values of Γ. Values for Γ ranged from 0 (the Dirac delta function) to 40 Hz. Between the values of 0 Hz and 0.825 Hz, Γ varied with a constant step size of 0.075 Hz. Between 0.825 Hz and 40 Hz, Γ increased with a variable step size that increased 10% per value. Before the convolution step in Eq. (5), each Lorentzian shape was truncated to span ±20 Hz and normalized. After computation, $S(TR, \delta_f, T_1, T_2, \Gamma)$ was decimated to 1-Hz resolution in δ_f values to reduce memory requirements. The final dictionary, consisting of 30 251 520 entries, spanned 101 values for δ_f that ranged from ±50 Hz. Dictionary generation was implemented in MATLAB (The MathWorks, Natick, MA) using custom-developed code.

3.3 | Pattern recognition

The inner-product-based pattern recognition method used in this work has been described previously.[12,13] For each pixel, the calculated dictionary and measured time course signals were normalized to their sum-squared magnitudes. The inner products between each pixel and dictionary entry was calculated, and the entry corresponding to the maximum value of the inner product was taken to represent the closest signal evolution to the acquired pixel. The estimated values for δ_f, T_1, T_2, and Γ were then derived from this entry. Relative proton density was derived from the scaling factor between the measured pixel signal and the matched dictionary entry. The value of T_2* for each pixel was calculated from match-derived T_2 and Γ values using Eq. (7).

3.4 | Phantom experiments

To evaluate the accuracy of qRF-MRF, a phantom study was performed. All studies were performed using a 16-channel head receiver array on a Siemens Magnetom Skyra 3T system (Siemens AG Medical Solutions, Erlangen, Germany). The accuracy of T_1 and T_2 were compared against traditional Cartesian spin-echo methods. Both phantom composition and traditional spin-echo methods have been described previously.[23] Briefly, the phantom consisted of 10 cylindrical compartments with different concentrations of gadopentate dimeglumine (Magnevist) and agarose (Sigma-Aldrich, St. Louis, MO). Reference T_1 values were measured using an inversion-recovery spin echo (8 log-spaced TIs ranging from 21 ms-3500 ms with 12-ms TE and 10-second TR). The T_2 values were measured using a repeated spin-echo sequence (7 log-spaced echoes that ranged from 13 ms-203 ms using a

TR of 10 seconds). Reference T_2* values used the multi-echo GRE method (25° FA excitation using 15 linearly spaced echoes ranging from 4 ms-152 ms with a TR of 200 ms). T_1 values were calculated pixel-wise by solving the equation $S(TI) = a + b\exp(-TI/T_1)$ using a 3-parameter nonlinear least-squares fitting routine. The T_2 values were determined pixel-wise by solving the equation $S(TE) = a\exp(-TE/T_2)$ using a 2-parameter nonlinear least-squares fitting routine. The T_2* values were fit similarly to T_2. The concordance correlation coefficient (CCC)[24] was used to assess measurement accuracy.

To assess how the number of frames affected quantification, the values for T_1, T_2, and T_2* were obtained from the dictionary pattern-recognition process using different numbers of frames. The number of frames was varied from 200–3000 frames with a 200-frame increment.

3.5 | In vivo experiments

In vivo volunteer brain data were acquired in an internal review board-approved study, with written informed consent obtained before each scan. The proposed qRF-MRF method was performed in five volunteers. For comparison of quantified δ_f, T_1, and T_2 properties, bSSFP-MRF[25] maps were acquired using 3000 time frames. For T_2* measurement validation, a multi-echo GRE method using Cartesian-based sampling (25° FA excitation using 11 echoes ranging from 4 ms-80 ms using a TR of 200 ms) was acquired. Quantified properties were assessed for each method in manually drawn regions of interest corresponding to the gray matter, white matter, the substantia nigra, and the red nucleus. The CCC[24] was used to assess agreement between quantified maps by qRF-MRF, bSSFP-MRF, and multi-echo GRE methods.

3.6 | Postprocessing

The postprocessing for all fingerprinting data was consistent with previous methods.[12] Acquired spiral data were reconstructed as described previously.[13] Briefly, the nonuniform fast Fourier transform,[26] using measured spiral trajectories,[27] was used to separately reconstruct each undersampled time frame from each coil. These frames were combined using the adaptive coil combination method.[28] Finally, all time frames were normalized to the combined coil sensitivity map.[29]

4 | RESULTS

Figure 3 shows example entries from the qRF-MRF dictionary. In each plot, the first 1800 of 3000 total frames of representative signal evolutions are shown. Shown in each subplot are seven signal evolutions that differ in only 1 of the 4 of the varied dictionary properties, δ_f, T_1, T_2 and Γ, while the other 3 properties are held constant. During the first 900 frames of the qRF-MRF method, changes in the shape of signal evolutions due to each property of δ_f, T_1, and T_2 are apparent. This is expected, as the FA, TR, and PH scheme in these frames are identical to bSSFP-MRF. However, only subtle differences can be observed due to variations of the Γ property. Starting from the 901st frame, a different scheme of low FA, constant TR, and quadratic PH starts. During these acquisition blocks, substantial signal shape variations can be observed due to δ_f, T_2, and Γ properties. As shown in Figure 3A, the frames with

high signal during qRF blocks depends on δ_f value. Despite the signal now arising from the sum of a distribution of δ_f values, high signal frames are still band-dependent. Changes in T_1 (Figure 3B) during qRF blocks are not as apparent as changes during bSSFP blocks. Changes in T_2*, either by a decrease in T_2 (Figure 3C) or increase in Γ value (Figure 3D), result in blunting of high-amplitude signal response during qRF blocks due to the dephasing.

Figure 4 shows the quantitative maps from phantom experiments. Figure 4A–E displays the maps obtained directly through the qRF-MRF dictionary-matching process. The δ_f map, shown in Figure 4A, shows substantial variation across the imaging FOV due to in-plane B_0 field inhomogeneity. For most phantom compartments, the δ_f variation was restricted between ±40 Hz. For these phantom compartments, T_1 and T_2 maps showed homogenous quantification. Pixels that mapped to +40 Hz in δ_f also showed errors in T_1 and T_2 quantification. This is due to the null-band behavior of bands for ±40 Hz during bSSFP acquisition blocks. The Γ maps were smooth within phantom compartments, but differed in spatial distribution as compared with T_1, T_2, or δ_f maps. The Γ in compositionally homogenous phantoms primarily represented the summed effects of in-plane and through-plane B_0 field inhomogeneity. The edges of phantom compartments, in which susceptibility differences near air interfaces can be expected to introduce intravoxel frequency variation, mapped to large matched Γ values. Relative M_0 maps calculated from the ratio between measured and matched signal evolutions are shown in Figure 4E. The relative M_0 map was smooth with the exception of pixels with propagated T_1 and T_2 errors at +40 Hz δ_f. Figure 4F shows the corresponding T_2* map. The reference multi-echo GRE T_2* map is shown in Figure 4G. The CCC between qRF-MRF-measured and GRE-measured T_2* maps was 0.90.

Figure 5 shows two example signal evolutions from the phantom experiment with superimposed corresponding matched fingerprints. Both signal evolutions originated from pixels within the same compartment. Dictionary matching of both signals obtained the same δ_f, T_1, and T_2 values but different Γ values, and thus different T_2* values, due to local variations in intravoxel B_0 field homogeneity. High-amplitude noise-appearing undersampling artifacts are apparent within the measured signal evolutions. However, the matching process was still able to recognize the best matching dictionary shape and extract the corresponding δ_f, T_1, T_2, and Γ properties.

Figure 6A–C shows the correlation of quantified T_1, T_2, and T_2* values obtained using all 3000 frames qRF-MRF against standard spin-echo and GRE methods, along with their corresponding linear regression, R^2 coefficient of determination, and concordance correlation results. Figure 6D–F shows the mean and SD of quantified T_1, T_2, and T_2* values according to the number of frames used in the matching process. Quantification of T_1 required fewer frames than T_2 and T_2* to accurately quantify. Dictionary matching using less than 900 frames, before the qRF acquisition blocks, showed unreliable T_2 and T_2* quantification. After the 900th frame, the SD of the T_2 and T_2* measurements decreased. Slight changes in the mean and SD of the quantification of T_1, T_2, and T_2* values was observed as the number of frames increased. Coefficient of variation, defined as the ratio between the SD and the mean of the measurements, for T_2* within each compartment is shown in Figure 6G. Due to differences in local B_0 inhomogeneity between phantom compartments, the coefficient of variation between compartments varied considerably

between compartments. However, within the same phantom compartment, the qRF-MRF and GRE methods showed comparable coefficient of variations, with the exception of the shortest T_2* compartment. In this compartment, the TEs used for the GRE method insufficiently covered the T_2* decay curve, which led to a variability in quantification.

Figure 7 shows representative reference bSSFP-MRF and qRF-MRF maps acquired in vivo. Visually, the qRF-MRF quantitative maps agreed well with maps from comparison bSSFP-MRF. The δ_f maps obtained using both qRF-MRF and bSSFP-MRF showed similar macroscopic B_0 field distributions. Vessels were visible in δ_f maps obtained by both bSSFP-MRF and qRF-MRF. Compared with bSSFP-MRF, the qRF-MRF δ_f map showed smoother matching results. Similar to phantom experiments, errors in T_1 and T_2 can be observed in pixels at ±40 Hz δ_f in both qRF-MRF and bSSFP-MRF methods. The CCCs between the shown bSSFP-MRF and qRF-MRF maps were 0.45 ± 0.11, 0.89 ± 0.03, and 0.60 ± 0.05 for δ_f, T_1, and T_2 properties, respectively. The CCC between all bSSFP-MRF and qRF-MRF maps was 0.35 ± 0.13, 0.83 ± 0.06, and 0.53 ± 0.11 for δ_f, T_1 and T_2 properties, respectively.

Figure 8 shows the qRF-MRF quantified T_2* maps, corresponding to the same images as in Figure 7, above their respective GRE T_2* maps. Vessels are visible in T_2* maps obtained by both GRE and qRF-MRF, due to the paramagnetic properties of iron in blood. The CCCs between the qRF-MRF and GRE-estimated T_2* maps was 0.82 ± 0.06 for the shown maps, and 0.77 ± 0.11 across all maps. The simultaneously acquired δ_f, T_1, T_2, relative M_0, and T_2* maps by qRF-MRF alongside the corresponding reference method acquired maps can be seen in Supporting Information Figure S1. Results of the region of interest analysis for in vivo δ_f, T_1, T_2, and T_2* values are listed in Table 1.

Quantitative Γ maps are shown in Figure 9A. Anatomical regions near air–tissue interfaces exhibited large Γ values. Blood vessels exhibited moderate Γ values. A zoomed-in Γ map of axial slice through midbrain structures is shown in Figure 9B. The corresponding T_2 and T_2* maps are reproduced in Figure 9C–F using a shared scale and color map. Higher Γ values and decreased T_2 and T_2* values within substantia nigra and red nucleus can be observed, due to higher tissue iron content within these tissues. The contrast of fine structures was preserved between qRF-MRF and reference maps.

5 | DISCUSSION

In this work, the proposed qRF-MRF method allowed the simultaneous quantification of δ_f, T_1, and T_2* tissue properties in 35 seconds per slice. The accuracy of the method was demonstrated in a phantom and in healthy volunteers. The ability to rapidly, robustly, and simultaneously quantify δ_f, T_1, T_2, relative M_0, and T_2* properties has many potential applications. For instance, through the knowledge of δ_f, T_1, T_2* and relative M_0 properties, synthetic SWI[30] may be possible, alongside synthetic T_1-weighted and T_2-weighted images that require knowledge of T_1, T_2, and relative M_0 properties. Another application lies in improving contrast agent sensitivity. Because MR contrast agents typically induce changes in multiple tissue T_1, T_2 and T'_2 properties, simultaneous detection of these properties may be able improve accuracy in contrast agents' detection and quantification.[31] Mapping of T_2 and T_2* tissue properties within midbrain structures may also enhance tissue iron

quantification. This may lead to the increased capacity to diagnose and monitor the diseases that are known to accumulate iron in these structures. However, the potential of the proposed qRF-MRF method for each of these applications must still be demonstrated.

The unique signal evolution that develops during qRF acquisition blocks has several beneficial properties for tissue property quantification. With respect to the components of T_2* quantification, the imaging frames with highest SNR also have the highest T_2 and Γ sensitivity. Additionally, qRF-MRF appeared to quantify δ_f more robustly as compared with bSSFP-MRF. Both in the current and previous[32] works, bSSFP-MRF, using direct pattern matching, was observed to be susceptible to locally discontinuous δ_f quantification errors. These errors had the potential to propagate to errors in T_1 and T_2 quantification. The qRF-MRF method appears to be more robust to this type of error.

Previously, a Cartesian EPI readout-based MRF method (MRF-EPI) was proposed for simultaneous measurement of T_1 and T_2* tissue properties.[33] The MRF-EPI method differed substantially from the current method in the use of a series of parallel imaging-based single-shot readouts with spoiled GRE acquisitions using variable FA, TE, and TR to generate image series that were sensitive to T_1 and T_2* values. Although the MRF-EPI method quantified relatively fewer tissue properties using a lower resolution and matrix size, MRF-EPI only required 10 seconds per slice. Future studies may seek to combine the approach of MRF-EPI with the current proposed method to further enhance robustness and speed of T_2* quantification.

Currently, the underlying frequency dispersion distribution during the dictionary-generation process was limited to Lorentzian shapes. This choice was made because simulation of a multi-echo GRE experiment would produce the consistent mono-exponential decay signal behavior assumed during GRE quantification. This assumption may not be accurate or appropriate in various situations. For instance, white matter has been shown to have a myelin signal component with both distinct rapid T_2* relaxation and substantial frequency shift.[34] Incorporation of the underlying causes of tissue-susceptibility differences due to vessel geometry or myelin into the signal model has previously been shown to enable potential quantification of these properties.[16,17,35] The qRF-MRF method may be sensitive to these properties as well. Although modeling these additional properties would result in an exponentially larger dictionary size, compression methods have been developed that may enable exploring this potential in the future.[36–39]

Several limitations remain in the proposed method. The first 900 frames of bSSFP-MRF were maintained at the beginning of the qRF-MRF acquisition. This was done because simulations showed decreased signal-shape differences with respect to changes in T_1 during qRF blocks as compared with bSSFP blocks. However, as a result of these high FA bSSFP blocks, the current qRF-MRF method was still susceptible to banding artifacts near ±40 Hz, coinciding with the off-resonance position of the bands during the first 900 frames, as shown in Figure 2D. Examples of these artifacts can clearly be seen in the phantom results (Figure 4B–D) corresponding to pixels with off-resonance value near 40 Hz (Figure 4A). Alternative banding-free schemes with sensitivity for T_1, such as FISP-MRF,[13] will be investigated in the future.

Another limitation of qRF blocks was the relative temporal sparseness of qRF-MRF signals as compared with bSSFP-MRF signals. The choices used in the current method were selected to increase incoherence of aliasing artifacts with respect to the signal evolution. The assessment of the number of frames necessary for accurate tissue-property measurements suggested that after approximately 2000 frames, accuracy of T_1, T_2, and T_2* quantification largely stabilized. However, matching precision improved up through the complete 3000 frames. Further improvements to accuracy and robustness may be made by optimizations to the acquisition parameters (FA, TR, and PH choices) or property estimation method, such as by adopting an iterative reconstruction method,[32,40–42] which may improve robustness to aliasing artifacts. These kinds of improvements would enable further reduction in acquisition time, by reducing the number of frames necessary for robust quantification.

Like all quantitative methods, property estimation depends on the accuracy of the underlying signal model. Although qRF-MRF quantification of T_1, T_2, and T_2* properties in phantom was shown to be accurate, several discrepancies appeared during in vivo experiments. Gray and white matter T_2 was consistently lower, as measured through qRF-MRF, as compared with both reference bSSFP and literature values. However, T_2* measurements in the same regions agreed well with the reference and literature values. Because T_2* is directly derived from quantified T_2 and Γ values, this suggests a corresponding underestimation of Γ values in gray and white matter. In one literature study, reports for R_2' values (theoretically related to Γ by scaled factor of π) varied from 2.7 s^{-1} to 3.5 s^{-1} for gray matter, and 2.8 s^{-1} to 4.3 s^{-1} for white matter, depending on the quantification method used.[43] Although none of the literature quantification methods can be considered a gold standard, the reported values appear to be consistent with an underestimation of Γ in gray and white matter in the current work. Several reasons may explain the accurate T_2* measurement yet biased T_2 and Γ measurements in vivo, which are not present in phantom experiments such as magnetization transfer effects.[44] Flow is another possible explanation, as none of the gradients used in the current method were flow compensated. Fresh spins flowing into the imaging plane likely have an additional effect on measured signal evolutions. Given that T_2 and Γ represent the irreversible and reversible components of signal decay, respectively, it is also likely that many other "irreversible" effects in vivo that are not currently in the signal model, including diffusion, motion, magnetization transfer, or eddy current effects, may manifest preferentially as an apparent shortening in T_2 value. These considerations are topics of careful future evaluation.

6 | CONCLUSIONS

In this work, we proposed a novel MR method, developed within the MRF framework, that can be used to simultaneously quantify δ_f, T_1, T_2, and T_2* properties. Using the flexibility of MRF experiment design, a quadratic RF phase was incorporated in a novel scheme to develop transient signals with high amplitude and a frequency-dependent phase. As a result, signals become uniquely sensitive to intravoxel susceptibility-induced field variation. Combined with Bloch equation-based template-matching approaches, intravoxel field variation can be estimated from measured signals, alongside other tissue properties. Accurate quantification of T_1, T_2, and T_2* tissue properties was achieved in phantom experiments at the current pixel sizes in 35 seconds per slice. In vivo experiments showed

robust and artifact-free property maps, with good agreement in T_2* quantification with the gold-standard multi-echo GRE method.

Supplementary Material

Refer to Web version on PubMed Central for supplementary material.

ACKNOWLEDGMENTS

This work made use of the High-Performance Computing Resource in the Core Facility for Advanced Research Computing at Case Western Reserve University.

Funding information

National Institute of Health (F30-HL124894, R01-EB017219, R01-DK098503, R01-EB016728, R01-EB023704, R01-HL073315, R01-HL094557, R21-HL126215, TL1-TR000441, and T32-EB007509) and Siemens Healthineers

REFERENCES

1. Gerlach M, Ben-Shachar D, Riederer P, Youdim M. Altered brain metabolism of iron as a cause of neurodegenerative diseases? J Neurochem. 2002;63:793–807.
2. Riederer P, Sofic E, Rausch WD, et al. Transition metals, ferritin, glutathione, and ascorbic acid in parkinsonian brains. J Neurochem. 1989;52:515–520. [PubMed: 2911028]
3. Chen JC, Hardy PA, Kucharczyk W, et al. MR of human postmortem brain tissue: correlative study between T2 and assays of iron and ferritin in Parkinson and Huntington disease. AJNR Am J Neuroradiol. 1993;14:275–281. [PubMed: 8456699]
4. Dexter DT, Carayon A, Javoy-Agid F, et al. Alterations in the levels of iron, ferritin and other trace metals in Parkinson's disease and other neurodegenerative diseases affecting the basal ganglia. Brain. 1991;114(Pt 4):1953–1975. [PubMed: 1832073]
5. Connor JR, Snyder BS, Beard JL, Fine RE, Mufson EJ. Regional distribution of iron and iron-regulatory proteins in the brain in aging and Alzheimer's disease. J Neurosci Res. 1992;31:327–335. [PubMed: 1573683]
6. Cornett CR, Markesbery WR, Ehmann WD. Imbalances of trace elements related to oxidative damage in Alzheimer's disease brain. Neurotoxicology. 1998;19:339–345. [PubMed: 9621340]
7. Kirk P, He T, Anderson LJ, et al. International reproducibility of single breathhold T2* MR for cardiac and liver iron assessment among five thalassemia centers. J Magn Reson Imaging. 2010;32:315–319. [PubMed: 20677256]
8. Lota AS, Gatehouse PD, Mohiaddin RH. T2 mapping and T2* imaging in heart failure. Heart Fail Rev. 2017;22:431–440. [PubMed: 28497231]
9. Bin NH, Song IC, Hyeon T. Inorganic nanoparticles for MRI contrast agents. Adv Mater. 2009;21:2133–2148.
10. Gelman N, Gorell JM, Barker PB, et al. MR imaging of human brain at 3.0 T: preliminary report on transverse relaxation rates and relation to estimated iron content. Radiology. 1999;210:759–767. [PubMed: 10207479]
11. Ma J, Wehrli FW. Method for image-based measurement of the reversible and irreversible contribution to the transverse-relaxation rate. J Magn Reson B. 1996;111:61–69. [PubMed: 8620286]
12. Ma D, Gulani V, Seiberlich N, et al. Magnetic resonance fingerprinting. Nature. 2013;495:187–192. [PubMed: 23486058]
13. Jiang Y, Ma D, Seiberlich N, Gulani V, Griswold MA. MR fingerprinting using fast imaging with steady state precession (FISP) with spiral readout. Magn Reson Med. 2015;74:1621–1631. [PubMed: 25491018]
14. Hamilton JI, Jiang Y, Chen Y, et al. MR fingerprinting for rapid quantification of myocardial T1, T2, and proton spin density. Magn Reson Med. 2017;77:1446–1458. [PubMed: 27038043]

15. Chen Y, Jiang Y, Pahwa S, et al. MR fingerprinting for rapid quantitative abdominal imaging. Radiology. 2016;279:278–286. [PubMed: 26794935]
16. Christen T, Pannetier NA, Ni WW, et al. MR vascular fingerprinting: a new approach to compute cerebral blood volume, mean vessel radius, and oxygenation maps in the human brain. NeuroImage. 2014;89:262–270. [PubMed: 24321559]
17. Lemasson B, Pannetier N, Coquery N, et al. MR vascular fingerprinting in stroke and brain tumors models. Sci Rep. 2016;6:37071. [PubMed: 27883015]
18. Assländer J, Glaser SJ, Hennig J. Pseudo steady-state free precession for MR-fingerprinting. Magn Reson Med. 2017;77:1151–1161. [PubMed: 27079826]
19. Scheffler K, Hennig J. Is TrueFISP a gradient-echo or a spin-echo sequence? Magn Reson Med. 2003;49:395–397. [PubMed: 12541263]
20. Gloor M, Scheffler K, Bieri O. Balanced SSFP. 2008;700:691–700.
21. Miller KL, Hargreaves BA, Lee J, Ress D, DeCharms RC, Pauly JM. Functional brain imaging using a blood oxygenation sensitive steady state. Magn Reson Med. 2003;50:675–683. [PubMed: 14523951]
22. Lee JH, Hargreaves BA, Hu BS, Nishimura DG. Fast 3D imaging using variable-density spiral trajectories with applications to limb perfusion. Magn Reson Med. 2003;50:1276–1285. [PubMed: 14648576]
23. Ma D, Coppo S, Chen Y, et al. Slice profile and B1 corrections in 2D magnetic resonance fingerprinting. Magn Reson Med. 2017;78:1781–1789. [PubMed: 28074530]
24. Lin LI. A concordance correlation coefficient to evaluate reproducibility. Biometrics. 1989;45:255–268. [PubMed: 2720055]
25. Badve C, Yu A, Rogers M, et al. Simultaneous T1 and T2 brain relaxometry in asymptomatic volunteers using magnetic resonance fingerprinting. Tomogr J Imaging Res. 2015;1:136–144.
26. Fessler JA, Sutton BP. Nonuniform fast fourier transforms using min-max interpolation. IEEE Trans Signal Process. 2003;51:560–574.
27. Duyn JH, Yang Y, Frank JA, van der Veen JW. Simple correction method for k-space trajectory deviations in MRI. J Magn Reson. 1998;132:150–153. [PubMed: 9615415]
28. Walsh DO, Gmitro AF, Marcellin MW. Adaptive reconstruction of phased array MR imagery. Magn Reson Med. 2000;43:682–690. [PubMed: 10800033]
29. Griswold M, Walsh D, Heidemann RM, Haase A, Jakob P. The use of an adaptive reconstruction for array coil sensitivity mapping and intensity normalization. In: Proceedings from the 10th Annual Meeting of ISMRM, Denver, CO; 2002: 2410.
30. Haacke EM, Mittal S, Wu Z, Neelavalli J, Cheng Y-CN. Susceptibility-weighted imaging: technical aspects and clinical applications, part 1. AJNR Am J Neuroradiol. 2009;30:19–30. [PubMed: 19039041]
31. Anderson CE, Donnola SB, Jiang Y, et al. Dual contrast-magnetic resonance fingerprinting (DC-MRF): a platform for simultaneous quantification of multiple MRI contrast agents. Sci Rep. 2017;7:8431. [PubMed: 28814732]
32. Pierre EY, Ma D, Chen Y, Badve C, Griswold MA. Multiscale reconstruction for MR fingerprinting. Magn Reson Med. 2016;75:2481–2492. [PubMed: 26132462]
33. Rieger B, Zimmer F, Zapp J, Weingärtner S, Schad LR. Magnetic resonance fingerprinting using echo-planar imaging: joint quantification of T1 and T2* relaxation times. Magn Reson Med. 2017;78:1724–1733. [PubMed: 27981641]
34. van Gelderen P, de Zwart JA, Lee J, Sati P, Reich DS, Duyn JH. Nonexponential T2* decay in white matter. Magn Reson Med. 2012;67:110–117. [PubMed: 21630352]
35. Miller KL, Smith SM, Jezzard P. Asymmetries of the balanced SSFP profile. Part II: White matter. Magn Reson Med. 2010;63:396–406. [PubMed: 20099329]
36. Cauley SF, Setsompop K, Ma D, et al. Fast group matching for MR fingerprinting reconstruction. Magn Reson Med. 2015;74:523–528. [PubMed: 25168690]
37. Ma D, Jiang Y, Chen Y, et al. Fast 3D magnetic resonance fingerprinting for a whole-brain coverage. Magn Reson Med. 2018;79:2190–2197. [PubMed: 28833436]

38. McGivney DF, Pierre E, Ma D, et al. SVD compression for magnetic resonance fingerprinting in the time domain. IEEE Trans Med Imaging. 2014;33:2311–2322. [PubMed: 25029380]
39. Yang M, Ma D, Jiang Y, et al. Low rank approximation methods for MR fingerprinting with large scale dictionaries. Magn Reson Med. 2018;79:2392–2400. [PubMed: 28804918]
40. Mazor G, Weizman L, Tal A, Eldar YC. Low rank magnetic resonance fingerprinting. In: Proceedings from the 38th Annual International Conference of the IEEE Engineering in Medicine and Biology Society, Orlando, FL; 2016: 439–442.
41. Doneva M, Amthor T, Koken P, Sommer K, Börnert P. Matrix completion-based reconstruction for undersampled magnetic resonance fingerprinting data. Magn Reson Imaging. 2017;41:41–52. [PubMed: 28223063]
42. Cline CC, Chen X, Mailhe B, et al. AIR-MRF: accelerated iterative reconstruction for magnetic resonance fingerprinting. Magn Reson Imaging. 2017;41:29–40. [PubMed: 28716682]
43. Ni W, Christen T, Zun Z, Zaharchuk G. Comparison of R2' measurement methods in the normal brain at 3 Tesla. Magn Reson Med. 2015;73:1228–1236. [PubMed: 24753286]
44. Bieri O, Scheffler K. On the origin of apparent low tissue signals in balanced SSFP. Magn Reson Med. 2006;56:1067–1074. [PubMed: 17036284]
45. Hasan KM, Walimuni IS, Kramer LA, Narayana PA. Human brain iron mapping using atlas-based T2 relaxometry. Magn Reson Med. 2012;67:731–739. [PubMed: 21702065]
46. Wansapura JP, Holland SK, Dunn RS, Ball WS. NMR relaxation times in the human brain at 3.0 tesla. J Magn Reson Imaging. 1999;9:531–538. [PubMed: 10232510]
47. Gelman N, Ewing JR, Gorell JM, Spickler EM, Solomon EG. Interregional variation of longitudinal relaxation rates in human brain at 3.0 T: relation to estimated iron and water contents. Magn Reson Med. 2001;45:71–79. [PubMed: 11146488]
48. Stikov N, Boudreau M, Levesque IR, Tardif CL, Barral JK, Pike GB. On the accuracy of T 1 mapping: searching for common ground. Magn Reson Med. 2015;73:514–522. [PubMed: 24578189]

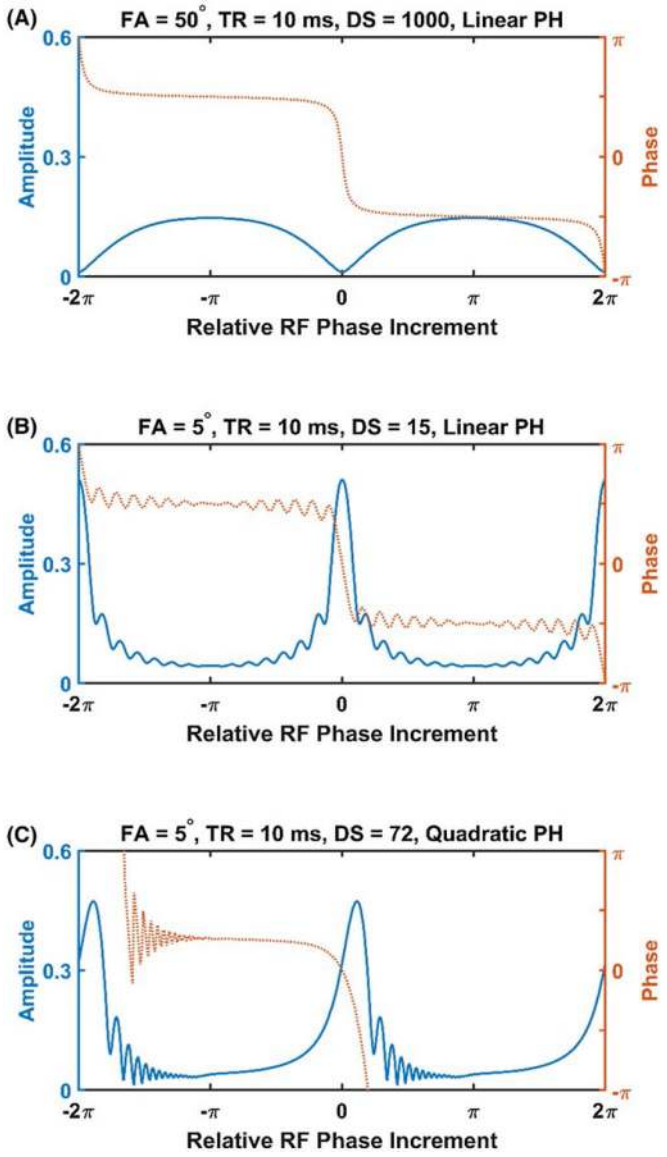

FIGURE 1.

Amplitude and phase responses during variations of balanced SSFP (bSSFP)-type sequences. Responses are plotted as functions of the relative phase increment between consecutive RF phase from a rotating reference frame locked to the isochromat precession frequency. Traditional bSSFP (A) with high flip angle (FA), many preparation dummy scans (DS), and linear RF phase increment (PH) generates high signal amplitude with flat phase response when PH increment is an odd multiple of π. Low FA bSSFP with low DS (B) shows high signal amplitude with steep phase response for PH increments near even multiples of π. Low FA with a quadratic PH evolution (C) shows a similar response profile as low-FA bSSFP. High amplitude and steep phase response is maintained regardless of DS number with quadratic RF phase

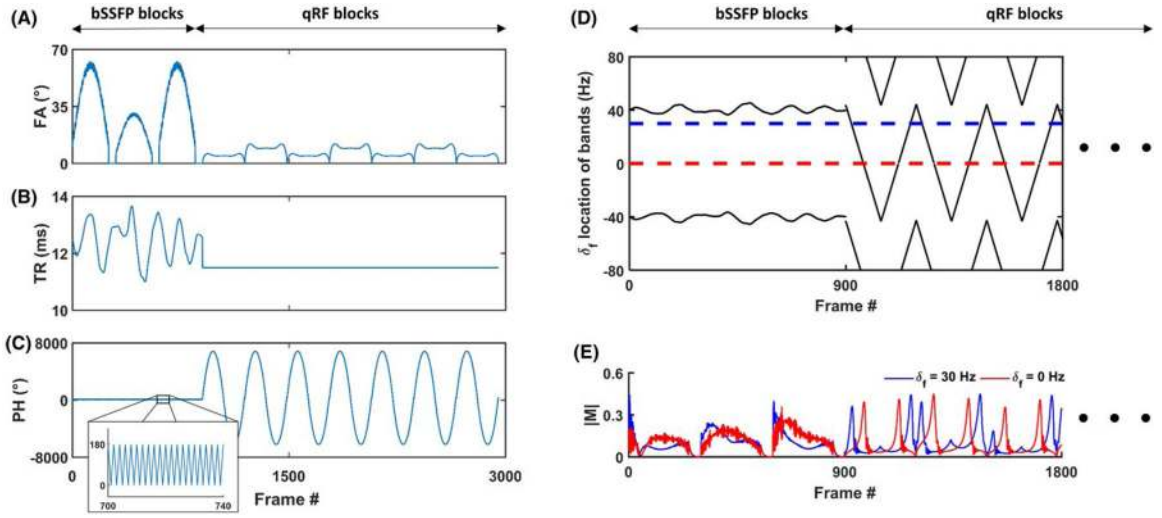

FIGURE 2.

Pulse sequence description. The FA (A), TR (B), and RF PH (C) used during acquisition of each time frame of the proposed method are shown. During the first 900 time frames, three bSSFP-based blocks of excitations are using parameters identical to previously established bSSFP-MRF, including the use of alternated phase cycling. During the latter 2100 time frames, seven quadratic RF (qRF) blocks of excitations are acquired using low FA, constant TR, and quadratic PH acquisition parameters. The resulting off-resonance frequency position of high T_2*-sensitive bands (D), calculated using Eq. (2), are shown for the first 1800 frames. Two example signal evolutions (E), differing only in δ_f value, are shown to illustrate signal behavior caused by the addition of quadratic phase RF. During quadratic RF lobes, high-amplitude signals from isochromats develop whenever resonance bands intersect the respective δ_f value

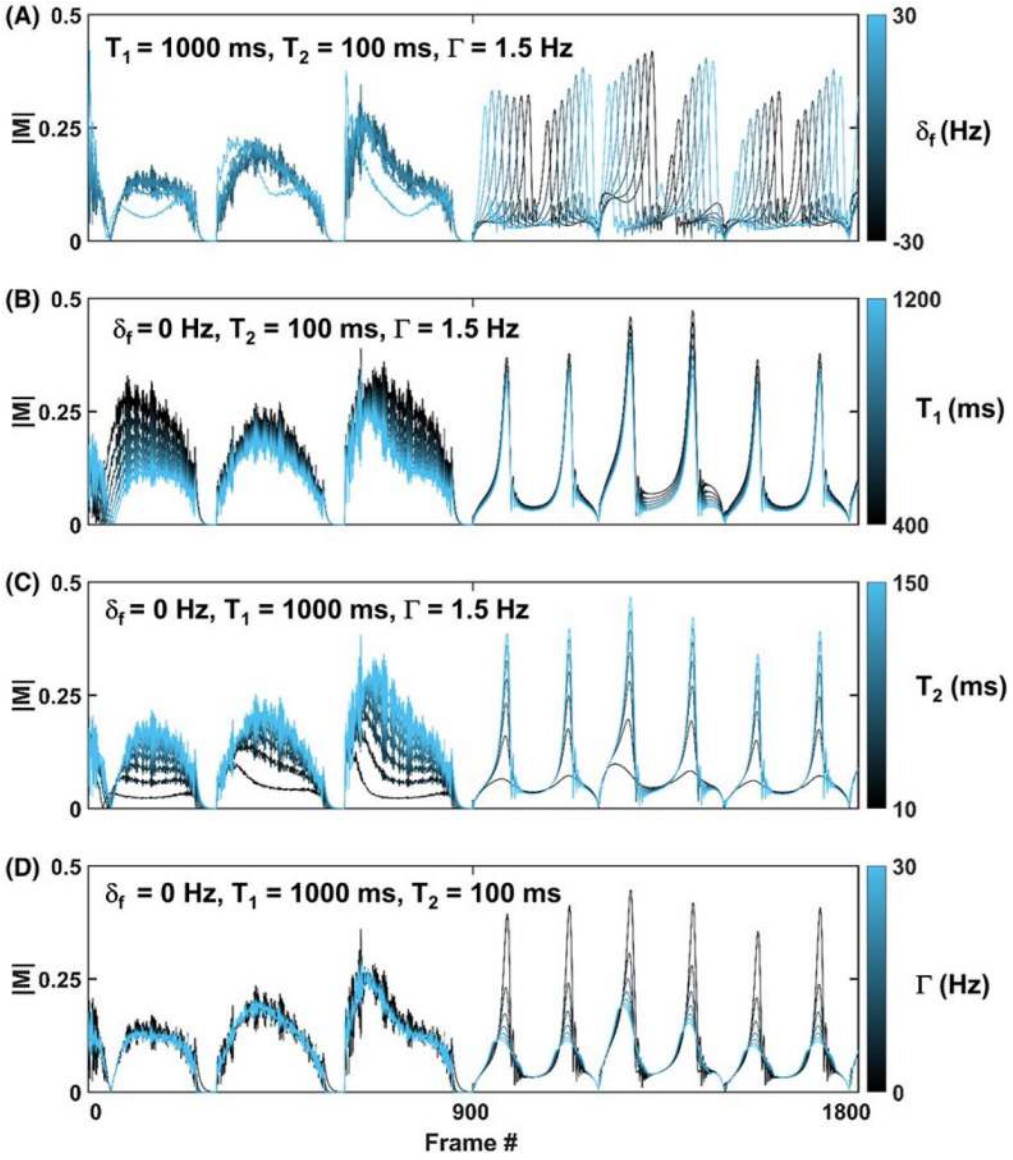

FIGURE 3.

Sets of representative dictionary entries. In each plot, only 1 of the 4 matched dictionary properties is varied (color bar), whereas the remaining 3 are fixed (values shown in insets). The 4 matched dictionary properties are δ_f(A), T_1 (B), T_2 (C), and intravoxel frequency dispersion Γ (D)

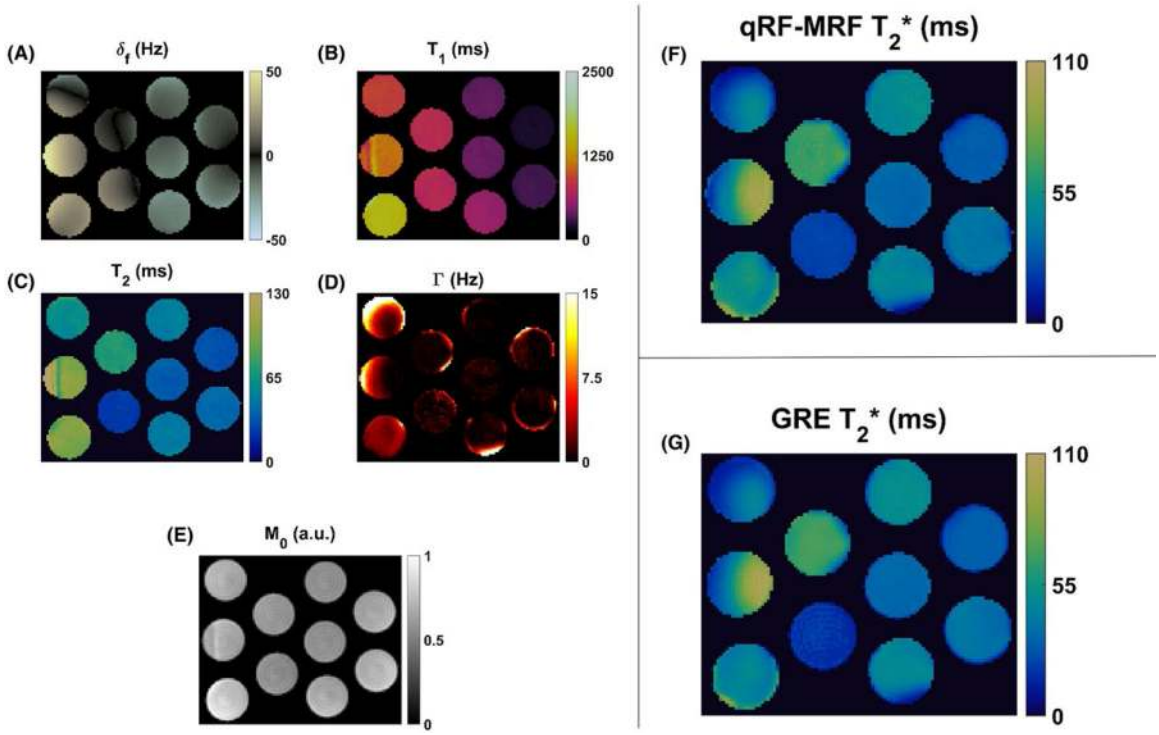

FIGURE 4.

Values of δ_f (A), T_1 (B), T_2 (C), Γ (D), and relative M_0 (E) are shown for phantom with varied concentrations of gadopentate dimeglumine and agarose generated using qRF-MRF. The resulting qRF-MRF T_2* map (F) shown was derived from T_2 and Γ maps using Eq. (7). The comparison multi-echo gradient-echo (GRE) quantified T_2* map (G) is also shown

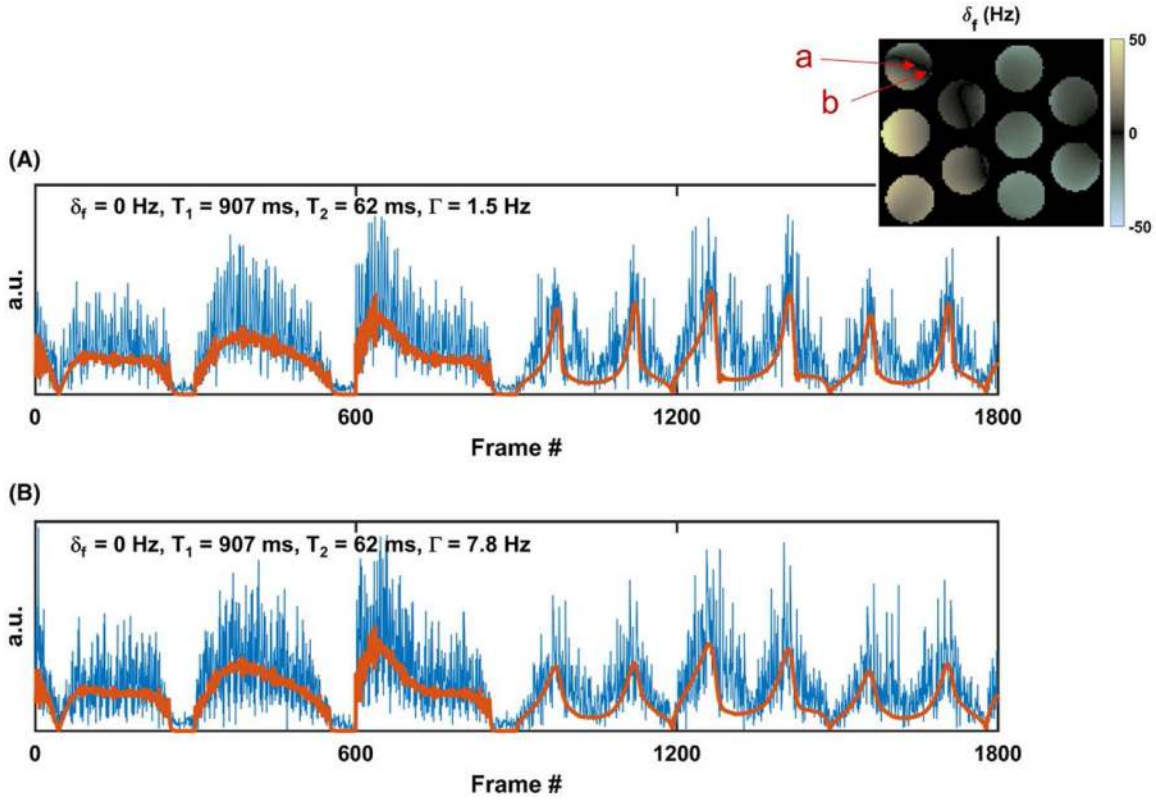

FIGURE 5.

Example undersampled time-frame data, with best matching dictionary entries, from two pixels originating within the same homogenous phantom compartment shown in Figure 4 (δ_f subfigure reproduced in inset). Differences in underlying signal shapes represent differences primarily caused by local field homogeneity within pixels. Property values extracted from the best dictionary matches are shown in inset

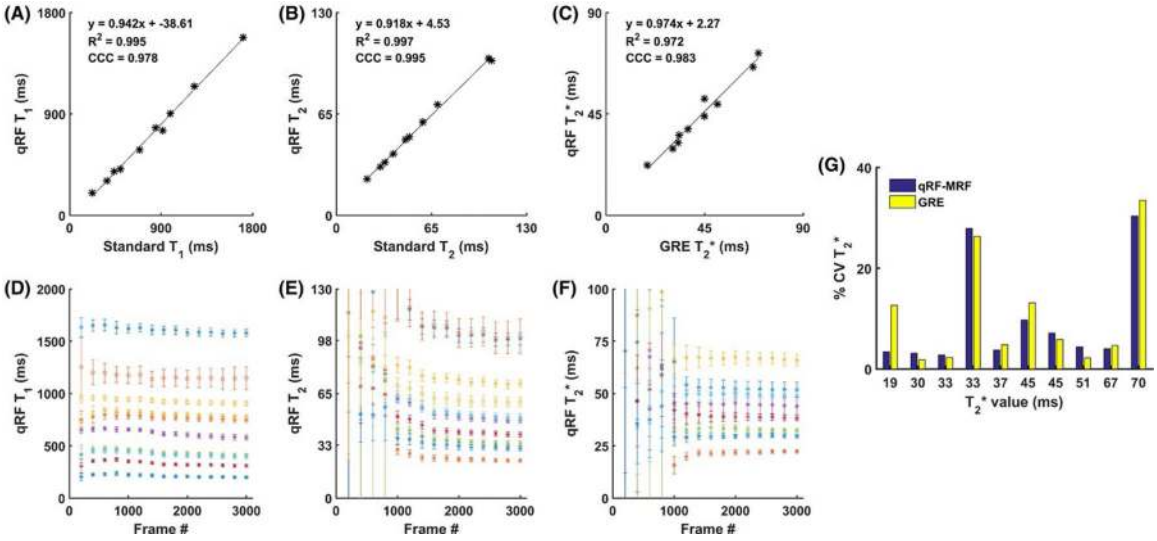

FIGURE 6.

Accuracy and reproducibility of qRF-MRF. The values of T_1 (A) and T_2 (B) values were measured within each phantom compartment using qRF-MRF against spin-echo methods. The T_2* (C) values were measured within each phantom compartment using qRF-MRF against the multi-echo GRE method. The mean and SD of T_1 (D), T_2 (E), and T_2* (F) measured within each compartment are shown with increasing number of time frames used during the dictionary-matching process. G, Coefficient of variation given by the SD divided by the mean, for T_2* measurement for both qRF-MRF and GRE methods against the GRE-measured mean T_2* value. The 2 compartments with large CV variation caused by poor local field homogeneity were excluded from (F) and plotted using circle markers in (D) and (E). Abbreviations: CCC, concordance correlation coefficient; CV, coefficient of variation

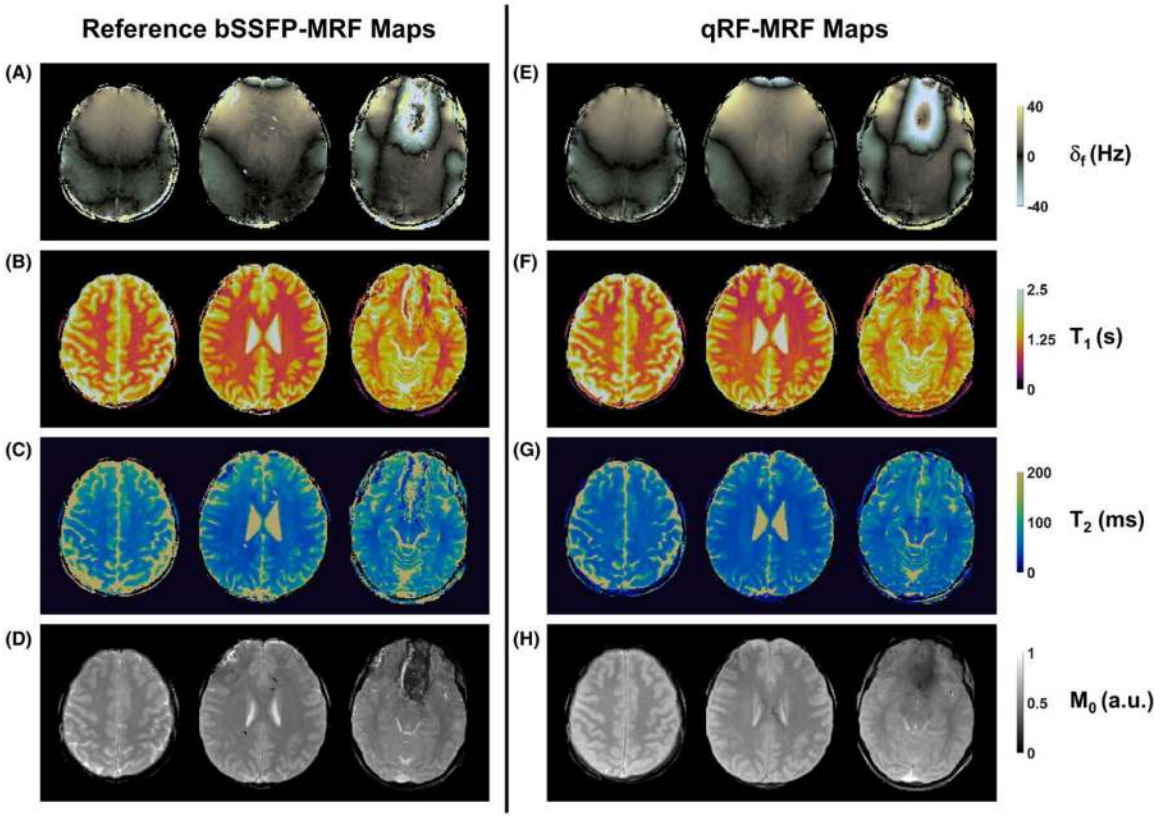

FIGURE 7.

Representative in vivo tissue property maps. Maps were acquired using both reference (left) and the qRF-MRF method (right) in healthy volunteers. Reference maps for δ_f(A), T_1 (B), T_2 (C), and relative M_0 (D) were generated using the bSSFP-MRF method with the same number of time frames as the qRF-MRF method. The qRF-MRF method simultaneously generated δ_f(E), T_1 (F), T_2 (G), and relative M_0 (H) maps are shown using the same scale as references maps. The total acquisition time for each scan was 38 seconds and 35 seconds per slice for each bSSFP-MRF and qRF-MRF scan, respectively

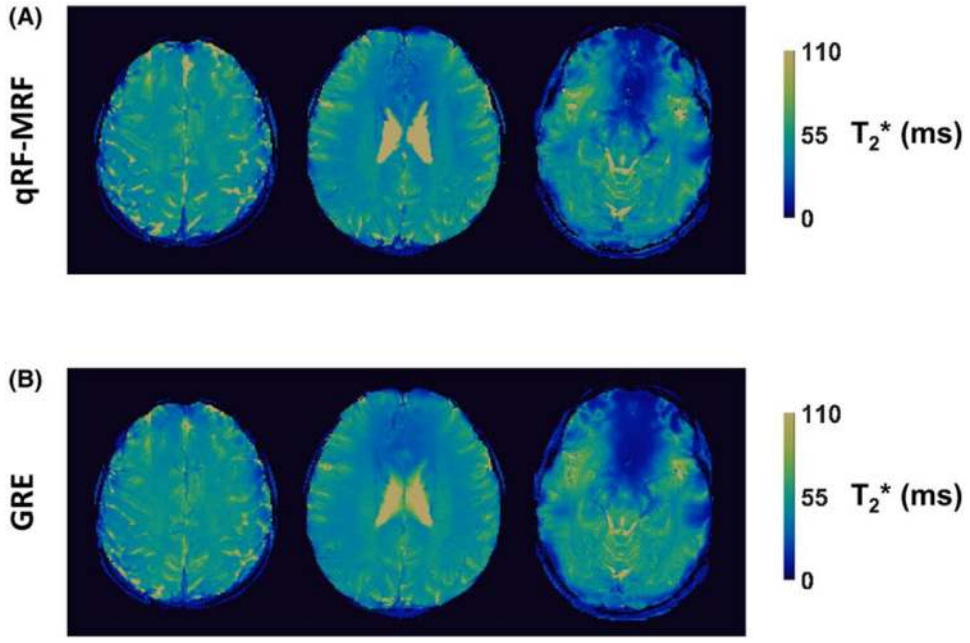

FIGURE 8.

Representative in vivo T_2* maps. The qRF-MRF T_2* maps (A), generated simultaneously with other tissue property maps shown in Figure 7, are shown above their corresponding multi-echo GRE-measured reference T_2* map (B). The GRE maps were acquired in 51 seconds each

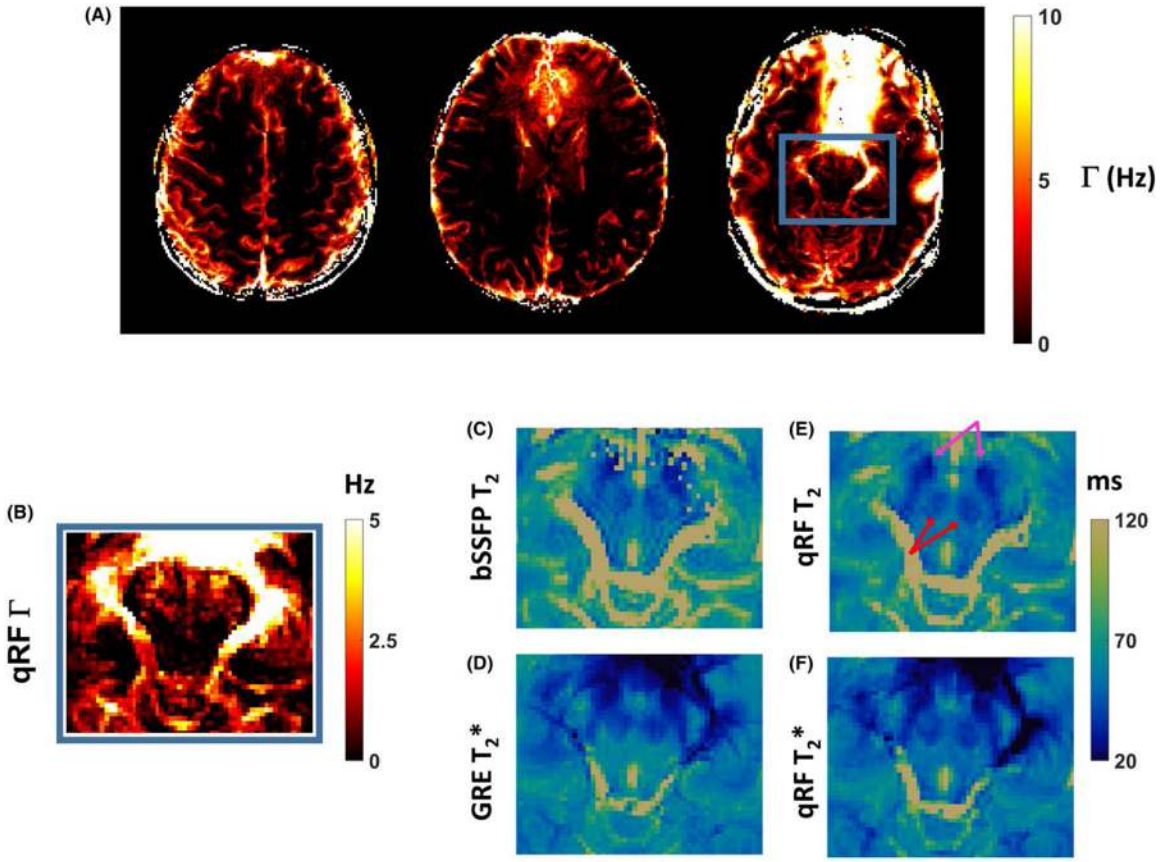

FIGURE 9.

A, The Γ maps acquired using the qRF-MRF method from the same experiments shown in Figures 7 and 8. B, Zoomed-in FOV of the Γ map to the midbrain structures. C,D, Corresponding zoomed maps from reference T_2 (C) and T_2* (D) maps. E-F, Corresponding zoomed maps from qRF-MRF-acquired T_2 (E) and T_2* (F) methods. The same scale and color map used for the T_2 and T_2* maps are shown. The lower T_2 value associated with substantia nigra (pink arrows) and red nucleus (red arrows) can be observed across all methods for both T_2 and T_2* values

TABLE 1

Region of interest analysis for in vivo T_1, T_2, and T_2* values

		qRF-MRF	Reference method[a]	Literature[10,13,45–48]
White matter (ms)	T_1	988 ± 66	917 ± 60	~690–1100
	T_2	44 ± 4	42 ± 5	~56–80
	T_2*	43 ± 4	46 ± 7	~45–48
Gray matter (ms)	T_1	1395 ± 227	1210 ± 351	~1286–1393
	T_2	63 ± 10	76 ± 9	~78–117
	T_2*	51 ± 9	49 ± 10	~42–52
Substantia nigra (ms)	T_1	1081 ± 69	978 ± 130	1147
	T_2	34 ± 2	38 ± 7	~42–47
	T_2*	25 ± 5	26 ± 6	~22–28
Red nucleus (ms)	T_1	1057 ± 97	958 ± 156	
	T_2	39 ± 6	42 ± 8	~46–48
	T_2*	32 ± 6	31 ± 6	~24–31

[a]Measured using bSSFP-MRF for T_1 and T_2 multi-echo GRE for T_2*.